

Supporting Information for

Ultrafast electron localization and screening in a transition metal dichalcogenide

Z. Schumacher¹, S. A. Sato^{2,3}, S. Neb¹, A. Niedermayr¹, L. Gallmann^{1,*}, A. Rubio^{3,4}, U. Keller^{1,*}

¹Department of Physics, ETH Zürich, 8093 Zürich, Switzerland

²Center for Computational Sciences, University of Tsukuba, Tsukuba, Ibaraki 305-8577, Japan

³Max Planck Institute for the Structure and Dynamics of Matter and Center for Free Electron Laser Science, 22761 Hamburg, Germany

⁴Center for Computational Quantum Physics (CCQ), Flatiron Institute, New York 10010, USA

*Corresponding authors.

Address: Institute of Quantum Electronics, ETH Hoenggerberg HPT E7.1, Auguste-Piccard-Hof 1, 8093 Zurich Switzerland

Phone: +41 44 633 3709

Email: gallmann@phys.ethz.ch, keller@phys.ethz.ch.

This PDF file includes:

Supporting text
Figures S1 to S7
SI References

Static absorption measurement

We performed static absorption measurements of our few-layer MoSe₂ films (6Carbon Technology) on 30 nm thick silicon nitride membranes from Agar Scientific (AGS171-1). For comparison, we also recorded static absorption data of mono layer samples from the same supplier. All data was taken in our attosecond transient absorption spectroscopy (ATAS) setup. The comparison is shown in Figure S1 below. The static absorption was measured in the range of 29 to 42 eV, where our setup delivers the highest flux. The data is limited to discrete energy intervals due to the harmonic structure of our XUV spectra. A static absorption measurement with similar fidelity around the Se edge was not possible due to the lower XUV count rate and the generally weaker absorption of Se at the relevant energy. The transient signal used for the ATAS scans overcomes these issues by fast averaging methods and the fact that only the difference in absorption between NIR excitation and ground state is measured. The strong signal from the excited sample further benefits the signal quality for the transient signal, while we cannot take advantage of this effect for the static measurements.

Estimates of sample excitation

Number of excited carriers. The number of excited carriers per pulse is obtained by using a model that was previously applied to other 2D materials (1). The carrier area density per pulse (cm⁻²) is given by:

$$n_0 = \frac{P\sigma}{Af_{rep}E}$$

with the average power P , the focal spot size A , the pulse repetition rate f_{rep} , the photon energy E , and the absorptance σ . A value of $\sigma = 0.03$ is used based on the dielectric constant (4) and sample geometry of MoSe₂. We obtain a carrier density of $1.95 \cdot 10^{14} \text{ cm}^{-2} \pm 0.75 \cdot 10^{14} \text{ cm}^{-2}$. The error bar is mainly due to uncertainties in the sample position within the focal spot. This carrier density is 1 to 2 orders of magnitude above the expected Mott density (2).

A similar estimate of carrier volume density can be obtained by using the fluence and absorption coefficient of MoSe₂ as presented by Zürich, et al. in 2017 (3). Here, the fluence F , the central frequency ν of the laser pulse, the absorption coefficient α , and the sample thickness is used. We find the carrier density therefore as follows:

$$N_e \cong \frac{F}{h\nu d} [1 - e^{-\alpha d}]$$

We estimate a carrier density in the range of $2.1 \cdot 10^{21} \text{ cm}^{-3} \pm 0.8 \cdot 10^{21} \text{ cm}^{-3}$ for an estimated sample thickness of 2 nm (3-4 layers). A sample thickness variation has a negligible effect compared to the uncertainty in fluence due to the sample position. A thickness of 3 nm would change the maximum carrier density by $0.023 \cdot 10^{21} \text{ cm}^{-3}$.

Estimation of bandgap renormalization. For the estimation of the bandgap renormalization, the method presented by Bennett et al. (4) is used:

$$\Delta E_g = \left(\frac{e}{2\pi\epsilon_0\epsilon_s} \right) \left(\frac{3}{\pi} \right)^{\frac{1}{3}} N_e$$

For MoSe₂ we use $\epsilon_s \approx 21.8$ (4) for the relative static dielectric constant, and the concentration of free electrons N_e calculated above. This results in a bandgap renormalization in the range of -187 meV to -143 meV, taking into account the uncertainty in carrier density.

Dynamics in the Se response

In the following, we discuss the dynamics observed in the signal obtained from the probe transition via the Se core level. Our data confirms observations that were previously reported for the closely related material MoTe₂ (5).

In figure 2b) of the main manuscript, lineouts of the spectral response for different delay times are shown. The prominent Mo peak above 35 eV decays with increasing time delay, while the response from the selenium transition is more complex. We concentrate here on the lower of the two derivative-shaped replica in the Se signal that arise from the two spin orbit split Se 3d core states. At first it might appear as if the valence band (VB) signal strength increases (first positive peak below 55 eV), suggesting an increased hole population in the valence band. However, we need to consider the simultaneously occurring effects of carrier thermalization and lattice heating to gain full insight. We therefore use a decomposition method to identify the contribution of band-filling, broadening and redshift of the absorption edge (3) to the measured transient spectrogram (see Fig. S2). Details on the decomposition approach are given below.

The band filling signal in Figure S2b shows the VB peak to narrow and move to higher energies, indicating a thermalization of the carriers to the top of the VB and bottom of the conduction band (CB), as expected for the initial non-thermal distribution. Simultaneously, we see a decay of the broad population of electrons in the conduction band within the first picosecond by the decrease of the amplitude of the higher CB (arrow above 56.5 eV). The broadening and red shift (Fig. S2c) leads to more absorption below the absorption edge and results in the overall increase of absorption in the VB as seen in the measurement. From these observations we can draw two important conclusions. First, carriers in the VB/CB thermalize within 800 fs (shift in energy of the VB peak) and recombine, as seen by the band filling signal. Second, the apparent initial increase in VB signal strength is due to a superposition of multiple effects and, thus, to gain the full insight into the carrier dynamics from the ATAS trace, a decomposition needs to be performed to disentangle the various competing processes similar to previous results (3, 5).

Decomposition of ATAS signal. The ATAS trace can be modelled using a static absorption spectrum, which is red shifted and broadened as well as combined with a state-blocking signal. We follow an adapted version of this reconstruction process, initially presented by Zürich et al. (3), as outlined below.

While it is preferred to use measured static absorption spectra for the input of the reconstruction, we must rely on calculated static spectra since the signal to noise of our static absorption data in the photon energy region of the Se transition does not allow for a robust decomposition of the signal from our thin MoSe₂ samples. We, therefore, calculate the static absorption spectrum for the Se transition based on the spin-orbit split core hole positions of 55.2 eV and 56.3 eV, respectively. The positions of the core hole energies are obtained by using the zero ΔOD crossing in the ATAS scan as the center between the VB and CB position for both pairs of positive and negative absorption bands in the Se signal. The values obtained with this method deviate slightly from literature values for Se core hole energies. The deviation could be due to the substrate affecting the MoSe₂ sample, The absorption spectrum is then obtained with the following model functional form and $\Delta E = 0.2$ eV:

$$A_{\text{static}}(E) = \frac{1}{1 + \exp(-(E - E_{\text{corehole}_1})/\Delta E)} + \frac{1}{1 + \exp(-(E - E_{\text{corehole}_2})/\Delta E)}$$

This static spectrum is then shifted and broadened by a convolution (denoted as * below) as follows:

$$\begin{aligned} \Delta A_{\text{shift}}(E) &= A_{\text{static}}(E) - A_{\text{static}}(E + E_{\text{shift}}) \\ \Delta A_{\text{broad}}(E) &= (A_{\text{static}}(E) * \exp(-E^2/(2\sigma^2))) - A_{\text{static}}(E) \end{aligned}$$

The initial band filling signal is calculated based on a gaussian distribution of holes/electrons in the VB/CB resulting in an increased/decreased absorption. Each distribution is calculated based on the following functional form (see Zürich et al. (3), SI. Eq. 7) :

$$\Delta A_{\text{band filling}}(E) = \exp\left(-\frac{4 \log(2)(E - E_{VB})^2}{BW_{\text{NIR}}^2}\right)$$

with E_{VB} the positions of the VB absorption features in the absorption spectrum and BW_{NIR}^2 the bandwidth of the NIR excitation. For the absorption features in the CB an analogous expression with opposite sign was used. For the excitation bandwidth, an initial starting value of 0.4 eV was assumed.

Two exemplary reconstructions at fixed delay times are shown in Fig. S3 and S4. The transient response is averaged for ± 30 fs around 100 and 800 fs, respectively. For these two time delays, we obtain reasonable agreement with the experimental data for a broadening of 0.3 and 0.6 eV for 100 and 800 fs, respectively. The observed shift increases from 0.2 eV at 100 fs to 0.4 eV at 800 fs.

We employed the same decomposition approach for the molybdenum transition at 34 to 44 eV. However, the reconstruction did not yield a good agreement with the experimental data (see fig. S5). This is further evidence that the signal from the Mo transition is dominated by the screening dynamics, which is not taken into account in the simple model underlying this decomposition.

Theory

First-principles electron dynamics calculation with time-dependent density functional theory (TDDFT). We analyze the microscopic electron dynamics in the material with first-principles electron dynamics calculations based on time-dependent density functional theory (6). Because the calculation method has been described in detail elsewhere (7), here, we only briefly describe the method for electron dynamics in MoSe₂. For practical calculations of electron dynamics, we solve the following time-dependent Kohn-Sham equation for electron orbitals:

$$i\hbar \frac{\partial}{\partial t} \psi_{bk}(\mathbf{r}, t) = \left[\frac{(\mathbf{p} + \mathbf{A}(t))^2}{2m_e} + \hat{v}_{ion} + v_H(\mathbf{r}, t) + v_{xc}(\mathbf{r}, t) \right] \psi_{bk}(\mathbf{r}, t), \quad (1)$$

where b is a band index, \mathbf{k} is the Bloch wavevector, and $\mathbf{A}(t)$ is a time-dependent vector potential, which is related to the external laser electric field as $\mathbf{E}(t) = -d\mathbf{A}(t)/dt$. The equation of motion, Eq. (1), contains the electron-ion interaction \hat{v}_{ion} , the Hartree-potential $v_H(\mathbf{r}, t)$, and the exchange-correlation potential $v_{xc}(\mathbf{r}, t)$. In this work, we employ the adiabatic local density approximation (ALDA) for $v_{xc}(\mathbf{r}, t)$ (8). To describe the electron-ion interaction, we employ the norm-conserving pseudopotential for both Mo and Se. For Mo, $4s$, $4p$, $4d$, and $5s$ electrons are treated as valence. For Se, we employ two sets of pseudopotentials. The first one is used to describe the excitations from semi-core states of Se, treating $3d$, $4s$, and $4p$ electrons as valence. The second one is used to describe the valence electron dynamics, treating $4s$ and $4p$ electrons as valence.

To analyze the optical property of the material, we compute the optical conductivity of the monolayer MoSe₂ with the first-principles electron dynamics calculation. For this purpose, we employ the real-time linear response calculation, by evaluating the electron dynamics with Eq. (1) under an impulsive distortion, $\mathbf{E}(t) = \mathbf{e}_x E_0 \delta(t)$. By using the induced current density $\mathbf{J}(t)$, the optical conductivity can be evaluated as

$$\sigma(\omega) = \frac{1}{E_0} \int_0^\infty dt \mathbf{e}_x \cdot \mathbf{J}(t) e^{i\omega t - \gamma t},$$

where γ is the damping parameter, which is set to 1.0 eV in this analysis. Please note that in reality the damping parameter depends on the probed transition. The use of a common single value leads to the observed discrepancy between theory and experiment in relative absorption strength of the Mo and Se features (see Figures 2b and 2c of the main manuscript).

To elucidate the modulation of the optical property of MoSe₂ by laser excitation, we compute the optical conductivity of the monolayer MoSe₂ with a hot-electron state, where the electron temperature is set to 0.5 eV, while the lattice remains cold (9). The result of the optical conductivity modulation with the electron temperature increase is shown in Fig. 2c) of the main text. Furthermore, the result with the independent-particle (IP) approximation, where the time-dependence of the Hartree and exchange-correlation potentials is ignored, is also shown in Fig. 2c) to demonstrate the important role of many-body effects.

We further analyze the microscopic mechanism of the modification of the optical absorption of MoSe₂ by decomposing the transient conductivity into the three components (7):

$$\Delta\sigma(\omega) = \Delta\sigma^{\text{BR}}(\omega) + \Delta\sigma^{\text{SB}}(\omega) + \Delta\sigma^{\text{LF}}(\omega),$$

where $\Delta\sigma^{\text{BR}}(\omega)$ is the contribution from the band renormalization, $\Delta\sigma^{\text{SB}}(\omega)$ is the contribution from the state-filling, and $\Delta\sigma^{\text{LF}}(\omega)$ is the local-field effect. The decomposed results and reconstructed data are shown in Fig. 3b) in the main text. A detailed description of the decomposition approach is provided in previous work (7).

To obtain further insight into the microscopic electron dynamics in MoSe₂, we compute the electron density dynamics under the irradiation of laser fields. We solve the time-dependent Kohn-Sham equation, Eq. (1), by employing a laser pulse. Here, we set the full duration of the laser pulse to 20 fs, the mean photon energy to 1.55 eV, and the peak field strength to 20 MV/cm. The initial electron density $\rho(\mathbf{r}, t = 0)$ is shown in Fig. 3a) in the main text along with the electron density difference $\delta\rho(\mathbf{r})$ induced by the laser excitation. Here, the electron density difference $\delta\rho(\mathbf{r})$ is evaluated as the average density difference, $\delta\rho(\mathbf{r}, t) = \rho(\mathbf{r}, t) - \rho(\mathbf{r}, t = 0)$ over 10 fs after the laser irradiation.

Orbital character of higher lying bands in Mo signal. To analyze the electronic structure of matter, we employ the density functional theory using the Quantum ESPRESSO package (10). Figure S6 displays the data shown in Fig. 1c) of the main manuscript over a wider energy range. The higher lying states that give rise to the broad derivative shaped feature at photon energies >43 eV in the Mo signal consist of a wide range of bound and delocalized states. The most dominant contribution comes from the Mo 5s orbital. This is also consistent with previous observations in MoS₂ using resonant photoemission (11). Clearly, *d*-orbital contributions play a negligible role in this energy window.

Projected density of states for Titanium. Figure S7 displays the projected density of states for titanium. The energy scale is referenced to the Fermi energy, which is located in the so-called giant

resonance of titanium. At those energies, the dominant contribution to the density of states comes from $3d$ orbitals. Only at about 5-6 eV above the Fermi energy, $3d$ and $4s$ orbitals contribute with similar strength.

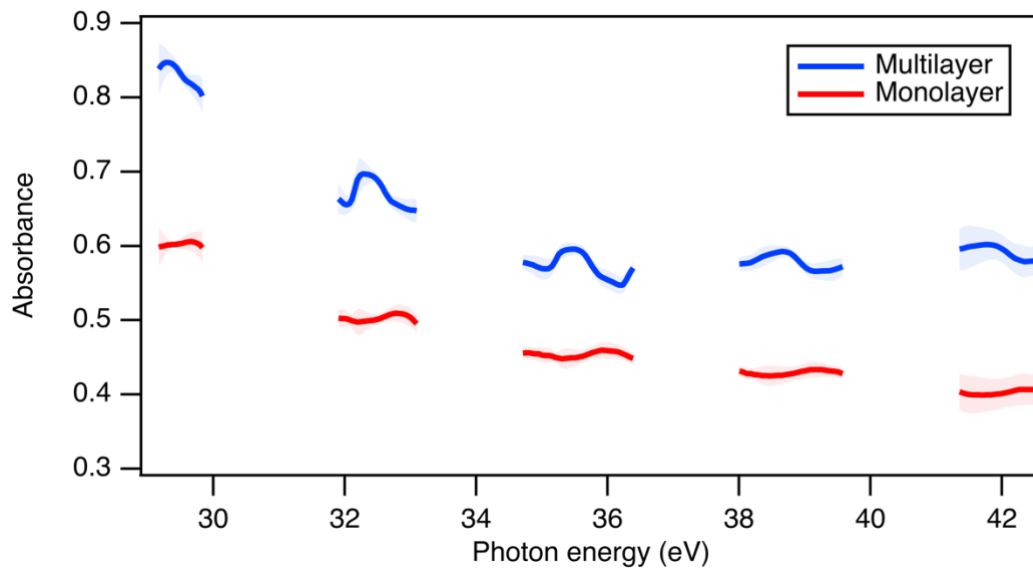


Figure S1. Static absorption measurement of mono- and multilayer MoSe₂. The discrete photon energy intervals are due to the harmonic spectrum of the probe XUV spectrum. The shaded areas represent the error bars (standard deviation over 3600 acquired sample and reference transmission spectra).

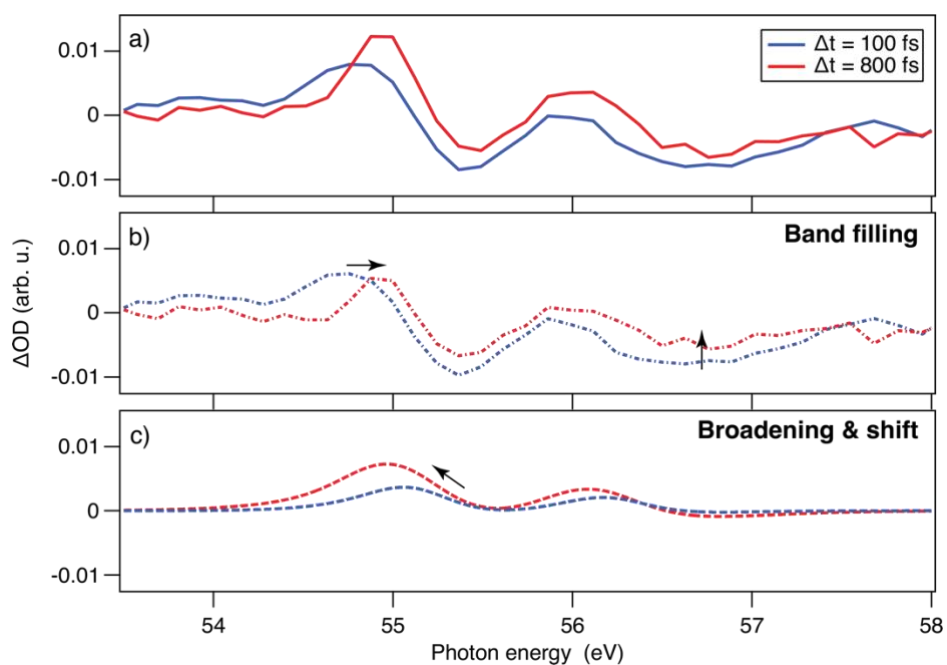


Figure S2. Evolution of the optical density change induced after photo excitation for Se core level to VB/CB. **a)** Measured change at two different pump-probe delays. **b)** The band filling and **c)** broadening & red shift contribution to the overall signal. Due to lattice heating, the latter contribution leads to an increase of the signal at 800 fs, resulting in an overall increase of the observed ΔOD at 55 eV.

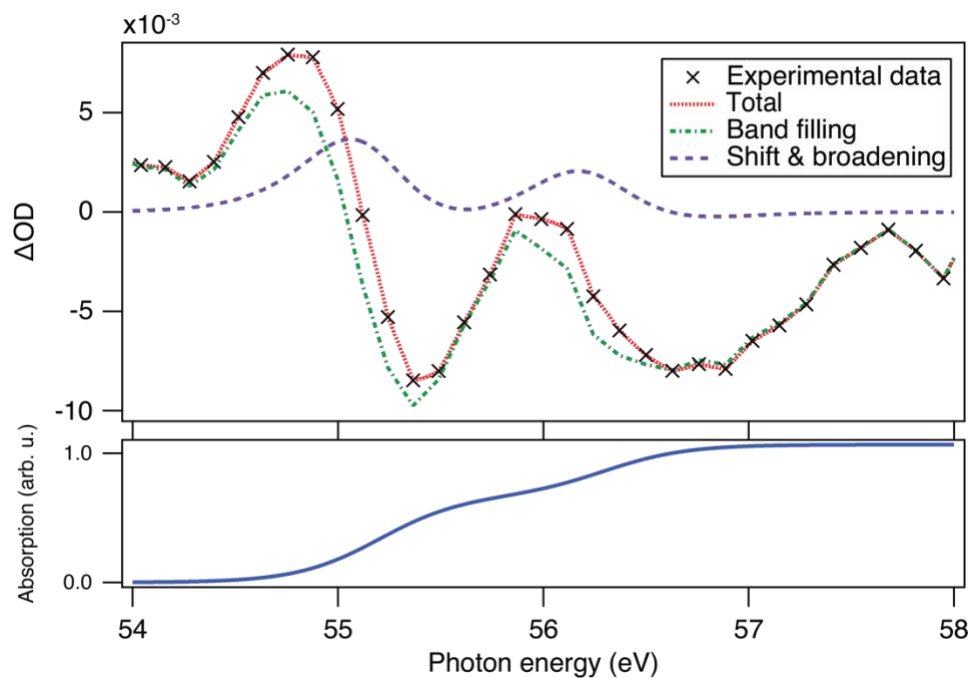


Figure S3. Decomposition of ATAS trace for the observed selenium transition at 100 ± 30 fs. The shift and broadening of the static absorption (bottom panel) is shown as a dashed purple line, with the band filling as a dash-dotted green line and the measured signal as black crosses. The red dotted trace shows the sum of the decomposed contributions.

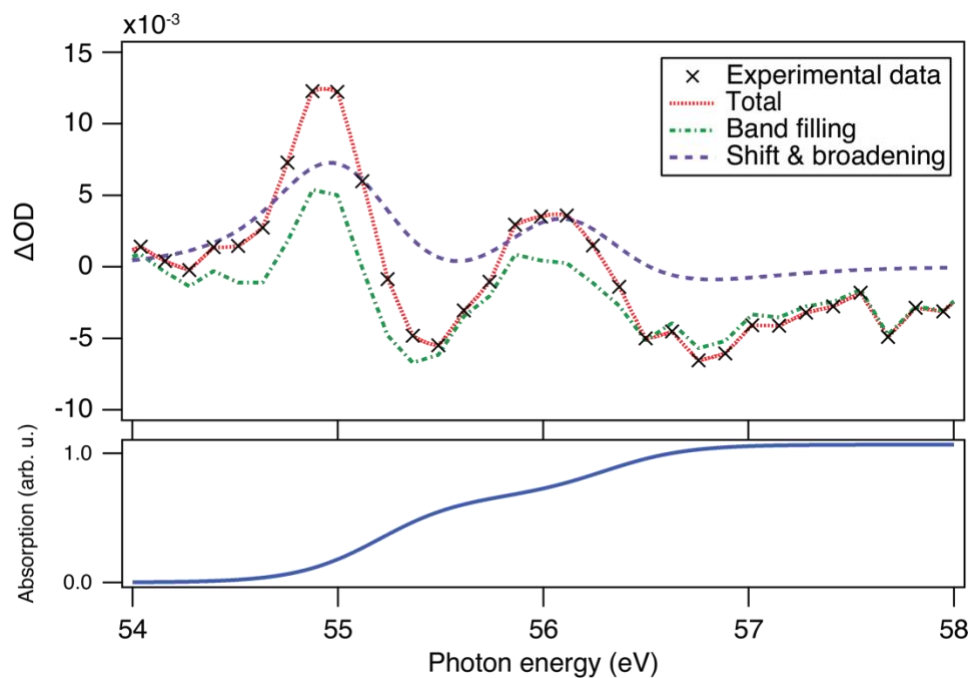


Figure S4. Same as Figure S3, but for a pump-probe delay of 800 ± 30 fs. The color code is identical to Figure S3.

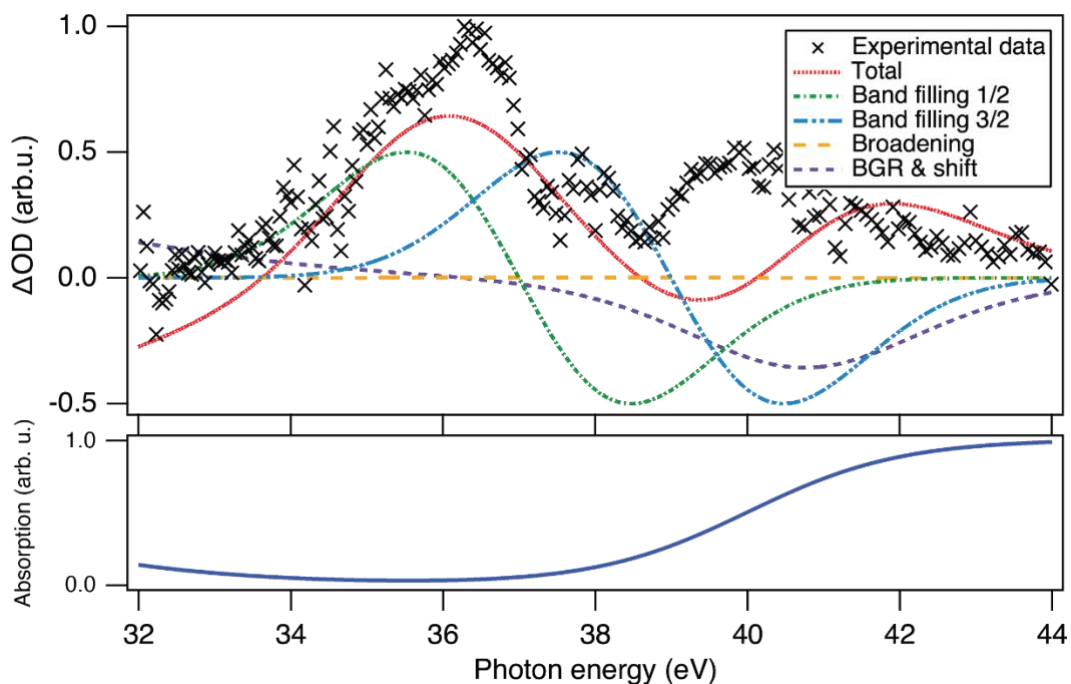


Figure S5. Attempted decomposition of ATAS trace for the observed molybdenum transition at a delay of 100 ± 30 fs. The total calculated signal (red dotted) does not agree well with the measured data (black crosses). This is further evidence that screening dynamics dominate the Mo response, which are not included in this model. The static absorption is shown in the bottom panel.

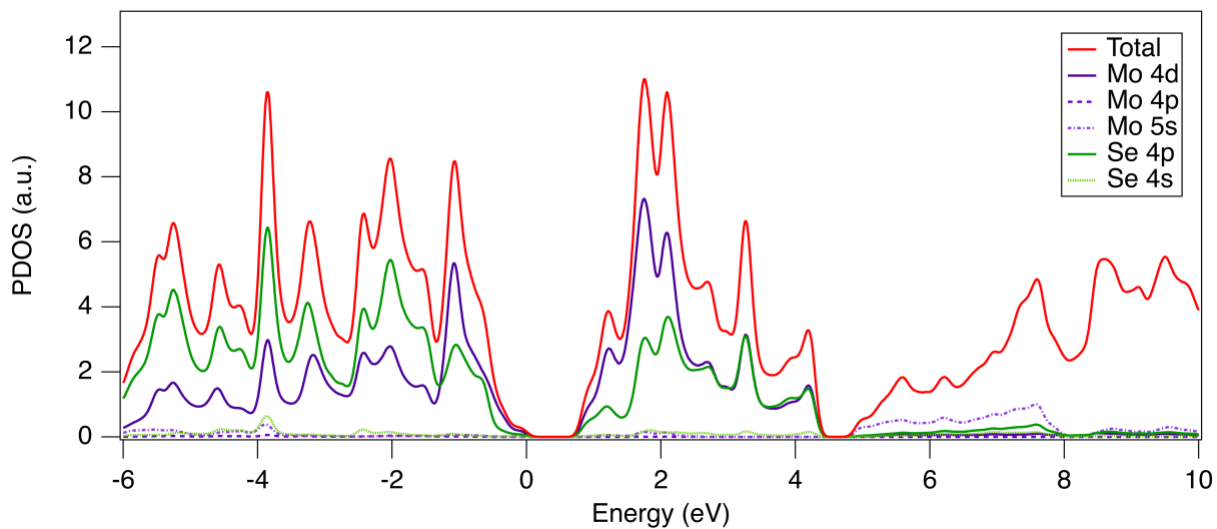


Figure S6. Projected density of states of bulk MoSe₂. This is an extended version of Fig. 1c, plotted over a wider energy range. In the band at energies of ~5 to >10 eV, contributions from *d*-orbitals play a minor role. Instead the Mo 5s orbital is the most dominant constituent among a multitude of other bound and delocalized states.

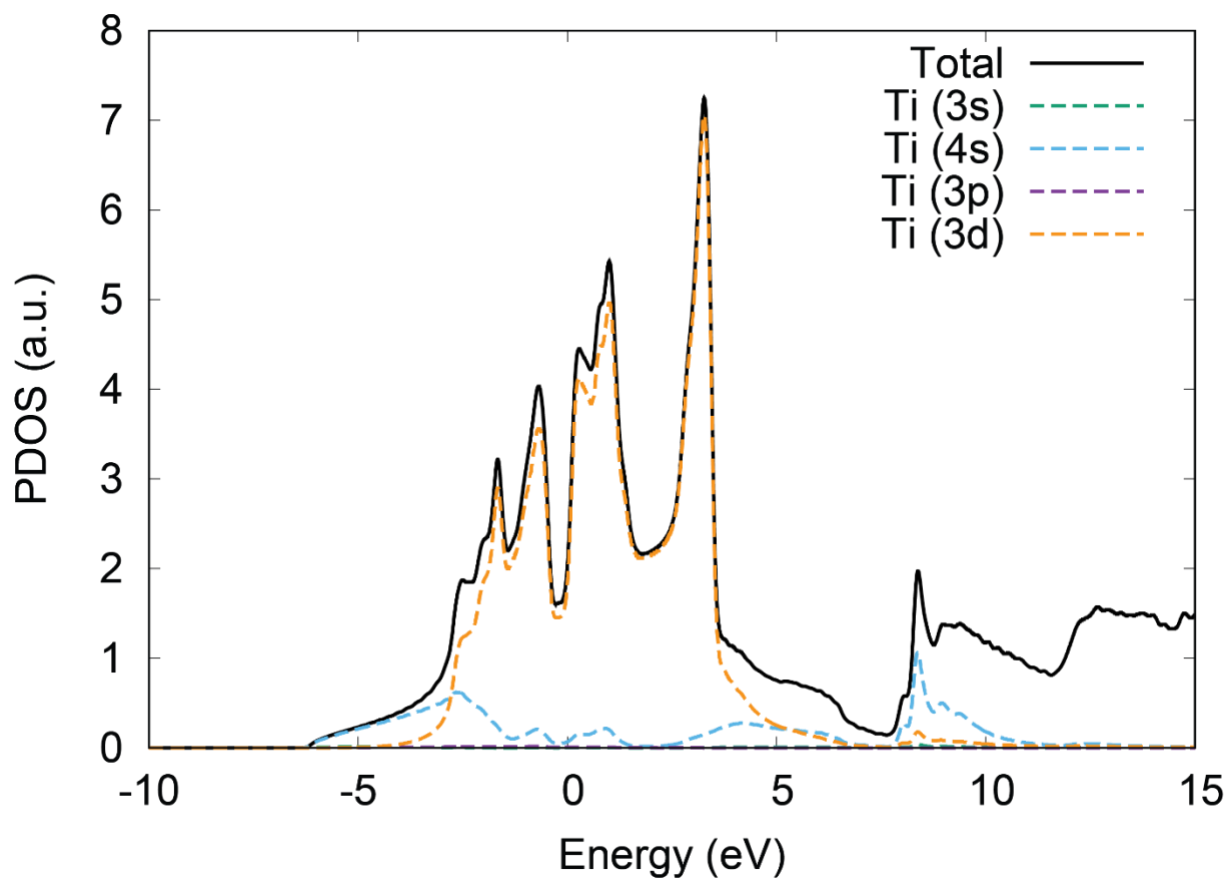


Figure S7. Projected density of states of titanium. In the region of the giant resonance around the Fermi energy, the density of states is dominated by 3d orbitals. About 6 eV above the Fermi energy, 3d and 4s states contribute with comparable strength.

SI References

1. J. Wang *et al.*, Optical generation of high carrier densities in 2D semiconductor heterobilayers. *Sci. Adv.* **5**, eaax0145 (2019).
2. L. Meckbach, T. Stroucken, S. W. Koch, Giant excitation induced bandgap renormalization in TMDC monolayers. *Appl. Phys. Lett.* **112**, 061104 (2018).
3. M. Zürch *et al.*, Direct and simultaneous observation of ultrafast electron and hole dynamics in germanium. *Nat. Commun.* **8**, 15734 (2017).
4. B. R. Bennett, R. A. Soref, J. A. D. Alamo, Carrier-induced change in refractive index of InP, GaAs and InGaAsP. *IEEE J. Quantum Electron.* **26**, 113–122 (1990).
5. A. R. Attar *et al.*, Simultaneous Observation of Carrier-Specific Redistribution and Coherent Lattice Dynamics in 2H-MoTe₂ with Femtosecond Core-Level Spectroscopy. *ACS Nano* **14**, 15829–15840 (2020).
6. E. Runge, E. K. U. Gross, Density-Functional Theory for Time-Dependent Systems. *Phys. Rev. Lett.* **52**, 997-1000 (1984).
7. S. A. Sato, First-principles calculations for attosecond electron dynamics in solids. *Comput. Mater. Sci.* **194**, 110274 (2021).
8. J. P. Perdew, Y. Wang, Accurate and simple analytic representation of the electron-gas correlation energy. *Phys. Rev. B* **45**, 13244 (1992).
9. S. A. Sato, Y. Shinohara, T. Otake, K. Yabana, Dielectric response of laser-excited silicon at finite electron temperature. *Phys. Rev. B* **90**, 174303 (2014).
10. P. Giannozzi *et al.*, Advanced capabilities for materials modelling with Quantum ESPRESSO. *J. Phys.: Condens. Matter* **29**, 465901 (2017).
11. J. R. Lince, S. V. Didziulis, J. A. Yarmoff, Resonant photoelectron spectroscopy at the Mo 4p → 4d absorption edge in MoS₂. *Phys. Rev. B* **43**, 4641–4647 (1991).